Contents lists available at ScienceDirect

Fire Safety Journal

journal homepage: www.elsevier.com/locate/firesaf

Temperature and heat flux measurements from firebrand piles using color ratio pyrometry ☆,☆☆

Elijah J. Igweh [a,b,c,*], Stanislav I. Stoliarov [a], Peter B. Sunderland [a]

[a] Department of Fire Protection Engineering, University of Maryland, College Park, USA
[b] International Master of Science in Fire Safety Engineering (IMFSE), Ghent University – UGent, Belgium
[c] Department for Research of Fire-Safe Sustainable Environment (FRISSBE), Slovenian National Building and Civil Engineering Institute (ZAG), Slovenia

ARTICLE INFO

Keywords:
Glowing embers
Wildland–Urban Interface fires
Smoldering
Image processing

ABSTRACT

Glowing firebrands are a key ignition source in Wildland–Urban Interface fires, yet their thermal characterization is challenging due to small size, irregular shape and sensitivity to environmental conditions. This study extends color ratio pyrometry from a single firebrand to firebrand piles to measure spatially resolved surface temperatures, heat flux to a remote location, and radiative loss fraction in a wind tunnel at 0.9–2.7 m/s. A Digital Single Lens Reflex camera, calibrated against a blackbody furnace, recorded temperatures at 1 Hz in the range 873–1473 K. Mean surface temperatures were measured with color ratio pyrometry and determined to be 1130–1260 K, with localized hot spots on the windward side of the pile. Radiant heat flux at a point 9.6 cm above the firebrand pile was computed using a pixel-wise view factor method with surface-specific emissivity and transmittance. This approach reproduced the temporal trends measured by a Schmidt–Boelter heat flux gauge, with peaks near 6 kW/m^2. Including a correction for hot, non-glowing regions below 873 K improved agreement across all wind speeds, keeping the average error below 9%. The radiative loss fraction, measured via carbon oxide calorimetry, stabilized at 0.20–0.23 during the first 100 s of the glowing phase.

1. Introduction

The frequency and severity of wildfires have increased in recent decades [1,2]. In Wildland–Urban Interface (WUI) fires, three primary ignition mechanisms are identified: radiant heat, direct flame contact, and firebrands, with firebrands as the dominant ignition source [3–5]. Field observations and laboratory experiments have shown that firebrands can travel several kilometers and accumulate on vulnerable building components [4,6]. Recent studies demonstrated that wind strongly enhances combustion rate, surface temperatures, and heat fluxes of firebrands [7,8]. Wind tunnel experiments showed that pile structure and airflow govern heat flux levels and ignition probability [9,10]. However, little is known about temporal and spatial evolution of surface temperatures in firebrand piles, where the combustion behavior is also influenced by their bulk density, porosity and internal re-radiation effects [9,11].

Traditional temperature measurement techniques, such as thermocouples, are often limited when applied to firebrands due to their small size, mobility, irregular shapes, thermal contact resistance, and the effects of quenching. These limitations hinder reliable temperature measurements on burning surfaces, especially when they crack or recede during combustion [7,12,13]. Single-band or broadband infrared (IR) thermography requires the surface emissivity to be known or accurately estimated [13], although emissivity is not constant and can vary with temperature. Furthermore, IR cameras are often limited by low spatial resolution and high cost.

Color ratio pyrometry provides a non-intrusive method for determining surface temperatures using a calibrated Digital Single Lens Reflex (DSLR) camera. This technique overcomes many of the limitations of conventional IR and thermocouple-based measurements. It has been successfully applied in diverse fields, including combustion diagnostics, aerospace testing, and explosive fireball characterization [14–16]. More recently, the method has been adapted to wildfire-relevant studies, allowing temperature measurements of individual glowing embers and simulated flying firebrands, with results showing that wind

☆ This article is part of a Special issue entitled: 'FISJ_IAFSS 2026' published in Fire Safety Journal.

☆☆ The author [Stanislav Stoliarov A] is an editor of this journal. In accordance with policy, [Stanislav Stoliarov A] was blinded to the entire peer review process.

* Corresponding author at: Department for Research of Fire-Safe Sustainable Environment (FRISSBE), Slovenian National Building and Civil Engineering Institute (ZAG), Slovenia.

E-mail address: elijah.igweh@zag.si (E.J. Igweh).

https://doi.org/10.1016/j.firesaf.2026.104712
Received 24 September 2025; Received in revised form 2 February 2026; Accepted 8 March 2026

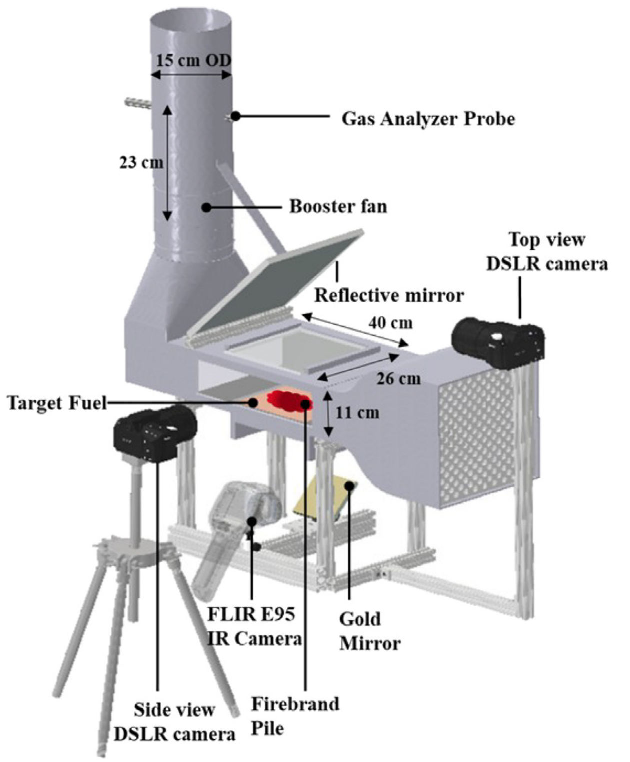

Fig. 1. A bench-scale wind tunnel setup used in this study drawn to scale. *Source:* Reproduced from Ref. [21].

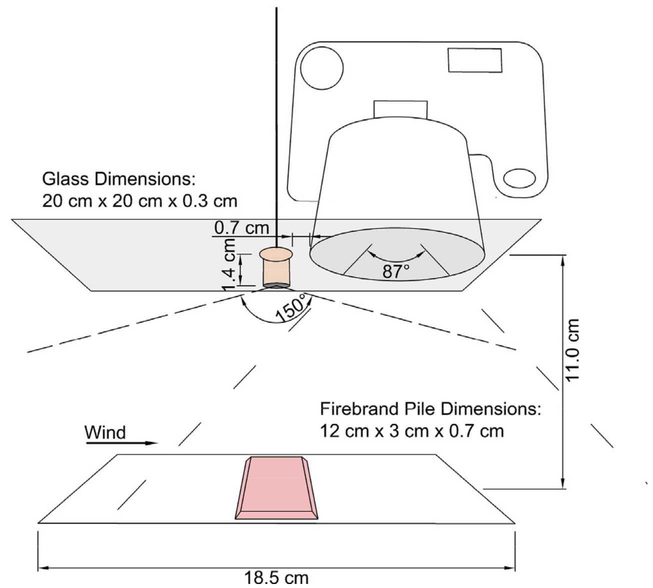

Fig. 2. Wind tunnel test section with camera (72 mm diameter) and heat flux gauge (9.52 mm diameter), including firebrand placement.

speed can significantly increase ember temperatures and combustion intensity [13,17–20]. In practical applications, color ratio pyrometry may be used to detect incipient fires and to assess the intensity of smoldering combustion. To advance these applications, future work should investigate larger scales, the influence of firebrand sizes, the effects of external light, and flame and smoke interference.

In this study, color ratio pyrometry is extended from single firebrands to a large number of glowing particles. Flaming combustion is not considered. For the first time, these spatially resolved temperature distributions are combined with heat flux measurements. The resulting temperature maps serve as the basis for heat flux determination at a distance, calculated through a pixel-by-pixel view factor analysis and validated against a remotely positioned water-cooled gauge.

2. Experimental

2.1. Wind tunnel apparatus and instrumentation

In this study, a modified bench-scale wind tunnel, based on the design by De Beer et al. [10,21] and Lauterbach et al. [22], was used as shown in Fig. 1. The tunnel includes a contraction cone, test section and exhaust system. The airflow was conditioned using a multi-layer honeycomb mesh (27 × 26 cm inlet), ensuring uniform and laminar airflow [23]. The cone reduces in height to 10 cm while maintaining a constant width of 26 cm. Firebrand piles were placed on a square sample holder (18.5 × 18.5 cm) within the 37 cm long test section as presented in Fig. 2.

The original top mirror of the tunnel [21] was removed, and the borosilicate glass window of the 20 × 20 cm top opening was replaced by one with a central opening to accommodate a 9.52 mm diameter water-cooled Schmidt–Boelter heat flux gauge (HFG). The HFG was mounted centrally above the firebrand pile, with its surface coated in high-emissivity paint (emissivity (ε) = 0.94) and calibrated against a reference gauge by the National Institute of Standards and Technology (NIST). The HFG was continuously water cooled throughout calibration and testing, with a flow rate of 1.25 l/min and a supply water temperature of 18 °C. The documented uncertainty of Schmidt–Boelter gauges is 8% [24]. A calibrated DSLR camera was positioned adjacent to the gauge for pyrometry measurements as shown in Fig. 2. This configuration ensures that both methods capture the entire hot region within the test section. The front glass panel permitted continuous observation.

Downstream of the test section, an exhaust system equipped with a TerraBloom DBF6 high-temperature booster fan (diameter 15.24 cm) controlled the wind speed in the tunnel from 0.5 to 2.9 m/s. Within the exhaust, a orifice-probe (72 holes, each with a diameter of 0.95 cm) was connected to a California Analytical Instruments ZPA non-dispersive infrared gas analyzer to measure Carbon Dioxide (CO_2) and Carbon Monoxide (CO) concentrations for Heat Release Rate (HRR) determination.

Firebrands used in the experiments were fabricated from cylindrical birch wood dowels (American Woodcrafter), each with an outer diameter of 6.35 mm, a length of 25.4 mm, and an approximate mass of 0.43 ± 0.02 g. The firebrands were placed at the center of a 0.32 cm thick, non-combustible ceramic fiber board, Kaowool Millboard 1401 (Thermal Ceramics). The board surface has an emissivity of ε = 0.62 [10]. To estimate the heating of the Kaowool board, two type K thermocouples were installed on the board surface at 3 cm and 4.5 cm on either side of the pile centerline as shown in Fig. 3. They were inserted from the underside and mounted flush with the surface using Autocrete HI-Temp ceramic adhesive. To minimize light reflections from glowing firebrands, two rectangular areas (3 × 14 cm) on the top surface of the Kaowool board were coated with high-temperature black paint (ε = 0.92), also covering the thermocouples.

2.2. Procedure

Wooden dowels for the firebrand generation were placed in a convection oven at 103 °C ± 2 °C for 24 h, per ASTM 4442-20 [25] and stored in an airtight resealable bag until the experiment is conducted. Glowing firebrands from wooden dowels were generated on a wire mesh pan above a propane flame (1.85 L/min, 40 s). After the propane was turned off, the dowels continued to burn until the self-sustained flames extinguished. The glowing firebrands were then transferred and

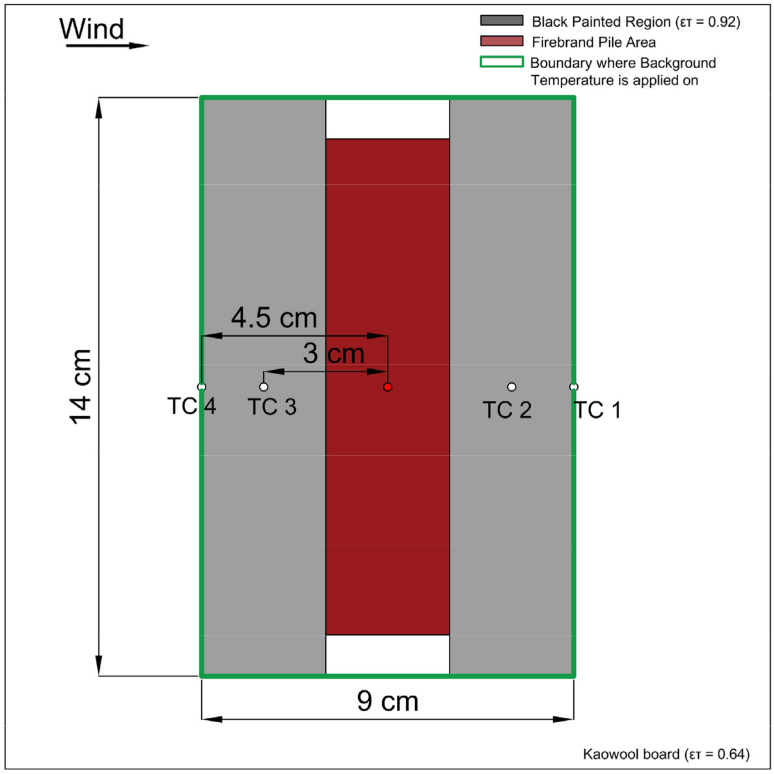

Fig. 3. Schematic illustration of the Kaowool board (white, $\varepsilon = 0.64$) showing the locations of the four thermocouples (TC 1–TC 4), the black-painted regions with high-emissivity coating (gray, $\varepsilon = 0.92$), and the designated firebrand placement area (red). The green boundary marks the region where the background temperature was applied in subsequent calculations.

placed onto the Kaowool board over a rectangular area measuring 12 cm in length and 3 cm in width, using a custom-built funnel. To promote near-uniform exposure to airflow across the surface while ensuring sufficient mass, the rectangular pile was prepared with a mass per area of approximately 0.06 g/cm^2. The pile was configured to resemble a single-layer arrangement of firebrands [22]. Based on these dimensions, the resulting pile height ranged from 0.7 to 1.0 cm, with a total mass of 2.2 g per experiment. The test section was subsequently sealed with a borosilicate glass plate. A total of 16 tests were performed, comprising four repetitions at wind speeds of 0.9, 1.4, 2.4, and 2.7 m/s. This range was selected for consistency with previous firebrand studies [10,22], with the highest wind speed constrained by the practical limitation of the booster fan and the increased tendency for firebrand displacement.

2.3. Camera calibration

Images were acquired using a Sony DSC-RX10MIII digital camera with an integrated ZEISS Vario-Sonnar T* lens with 72 mm filter thread, set to a focal length of 24 mm, an aperture of f/5.6, and an International Organization for Standardization (ISO) number of 200. The camera has a 20.1 MP Exmor RS CMOS sensor (13.2 × 8.8 mm) with 14-bit depth per channel [26]. To eliminate automatic corrections and ensure repeatability across all trials and previous studies [13], the digital camera was operated in Manual Exposure mode. RAW images (.ARW) were recorded at 5472 × 3648 pixels. White balance was fixed to daylight, and long-exposure noise reduction was disabled, although these settings do not affect RAW pixel values. Exposure compensation was set to 0 EV. Focus was fixed at 0.2 m for sharp imaging of the firebrand pile. Images were triggered at 1 Hz using an Arduino UNO microcontroller, while shutter speed was adjusted according to wind speed to avoid pixel saturation and ensure sufficient brightness. The resulting exposure times are summarized in Table 1.

Table 1
Test conditions: Wind speed and corresponding camera exposure times.

Wind speed (m/s)	Exposure time (ms)
0.9	12.5
1.4	6.25
2.4	5
2.7	5

The camera calibration for color ratio pyrometry was conducted using a blackbody furnace (Oriel 67032), which operates between 323 and 1473 K with an accuracy of ±0.2 K and emissivity of $\varepsilon = 0.99 \pm 0.01$. The camera was positioned directly in front of the 25.4 mm aperture. Images were captured at various shutter speeds, and a 200 × 200 pixel region was centered on the blackbody opening. To evaluate the accuracy of the calibration, the measured temperatures were compared with the predefined setpoints of the blackbody furnace under various camera settings within the calibration range of 873 to 1473 K. Additionally, the influence of a borosilicate glass window was investigated, showing a maximum deviation of ±13 K.

Color ratio pyrometry measures temperature based on emitted thermal radiation in the visible spectrum, using the spectral emissive power $E_{b,\lambda}$ of an ideal blackbody:

$$E_b(\lambda, T) = \frac{C_1}{\lambda^5[exp(C_2/\lambda T) - 1]}, \tag{1}$$

where $C_1 = 3.742{\times}10^8$ W $\frac{\mu m^4}{m^2}$, $C_2 = 1.439{\times}10^4$ μmK, λ is the wavelength, and T is the blackbody temperature.

Images were acquired in the three color channels: red, green, and blue, with peak wavelengths for the channels in the visible spectrum, ranging from 430 to 680 nm [13]. The camera response P_i to $E_g(\lambda, T)$

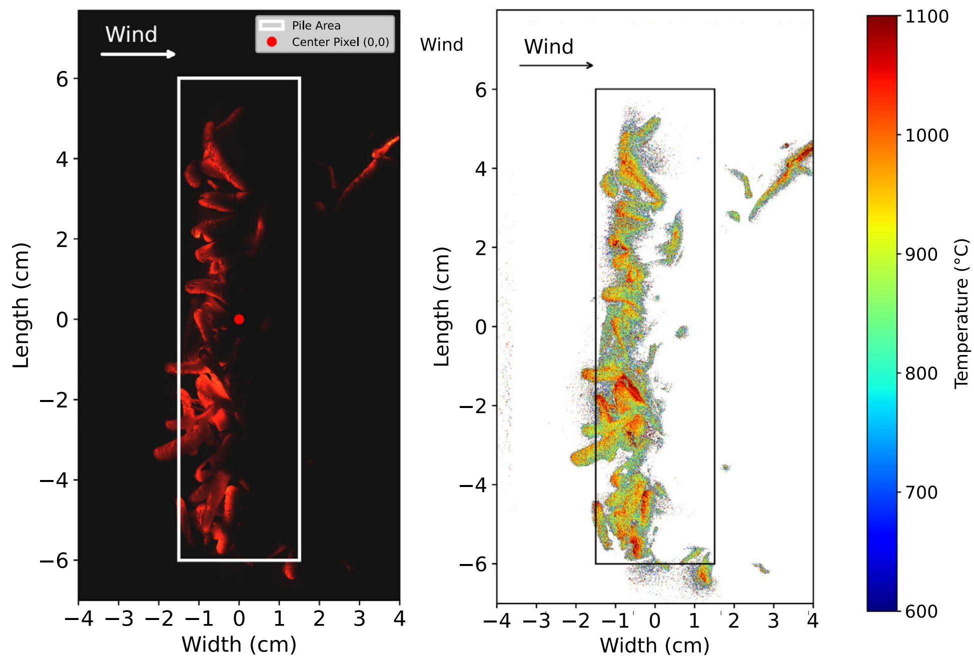

Fig. 4. Original TIFF image (left) and ratio pyrometry temperature distribution (right) at 2.7 m/s wind speed at 10 s. $t = 0$ s marks wind tunnel closure. Rectangle indicates the pile deposition area using a funnel.

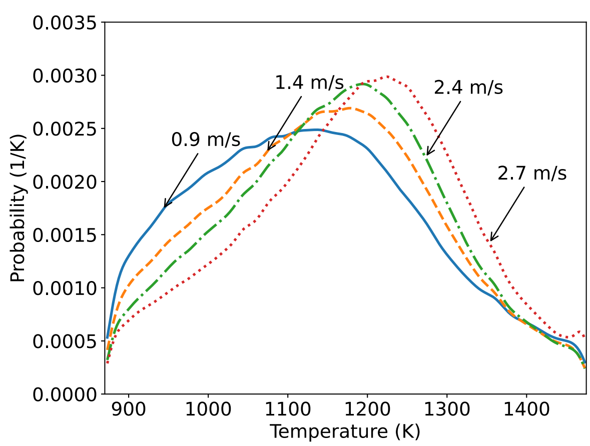

Fig. 5. Probability distribution of the glowing regions in the firebrand pile temperatures at $t = 10$ s for wind speeds from 0.9 to 2.7 m/s with a bin width of 10 °C. $t = 0$ s marks wind tunnel closure.

over the visible wavelength range can be expressed as [27]:

$$P_i = \Psi_i \Delta A_d \Delta\omega_d \; t \int_{430\,\text{nm}}^{680\,\text{nm}} \tau(\lambda) E_g(\lambda, T) \chi_i(\lambda)\, d\lambda, \tag{2}$$

where P_i is the camera's response for channel i (with i representing one of the red, green, or blue color channels); Ψ_i is the gain of the internal electronics; ΔA_d is the area of a single pixel on the camera sensor; $\Delta\omega_d$ is the solid angle of the pixel; t is the exposure time; $\tau(\lambda)$ is the transmissivity; and $\chi_i(\lambda)$ is the spectral sensitivity of the color filter.

Normalized pixel values (NI_i) were derived to account for variations in camera settings and is expressed as [13]:

$$NI_i = \frac{(I_i - I_{i,DC})\, f^2}{t\, ISO}, \tag{3}$$

where I_i denotes the pixel value of one of color channels (red, green, or blue), and $I_{i,DC}$ represents the dark current, which had negligibly small fluctuations over various exposure times.

Temperatures were derived using color ratio pyrometry performed on a pixel-by-pixel analysis. The ratio of normalized pixel values in the green and red channels (NI_G/NI_R) increases monotonically with temperature and provides a stable correlation for temperature measurements [13]. Compared to blue/green and blue/red ratios, it offers a higher signal-to-noise ratio. The uncertainty of ember pyrometry at each pixel is estimated at ±20 K [13,19]. The color ratio pyrometry was analyzed in Python to retrieve the temperature from NI_G/NI_R. First, dcraw [28], was used to convert the uncompressed RAW image into a 16-bit TIFF image at settings "-v", "-4", and "-T". Images were loaded into Python using the OpenCV library and information on exposure time, F-Number, and ISO were extracted.

Low-intensity pixels were identified when the red channel satisfies $I_{red} < 2\, I_{red,DC}$ and are set to null. To reduce artifacts from background reflections and camera noise, a spatial 50% rule was applied: within a 7 × 7 neighborhood, the center pixel was retained only if at least 25 surrounding pixels are valid; otherwise, it was set to null. All null pixel were identified as non-glowing within the image. These include: (1) cold areas of the Kaowool board, which were assigned an ambient temperature of 298 K, (2) non-glowing firebrands and (3) heated regions of the Kaowool board, which were accounted for using a mean background temperature profile estimated from thermocouple measurement on the board surface. The remaining non-null pixels, which correspond to hot firebrand regions, were converted to temperatures using the calibrated polynomial fit of the color ratio pyrometry. Hot regions within the blackbody calibration range of 873 to 1473 K were identified as glowing region. For pixels exceeding 1473 K, an additional filtering step was applied: If more than half of the surrounding pixels within a 7 × 7 neighborhood also exceed this threshold, the central pixel was assumed to belong to a high-temperature region and its value was capped at 1473 K. Otherwise, the pixel was replaced by the mean of valid neighboring values to reduce the impact of saturation and noise artifacts. This method enables the reliable extraction of regions that provide high-accuracy measurements through color-ratio pyrometry, while effectively excluding background areas. This pixel-by pixel approach is particularly beneficial for firebrand piles, whose position and shape varies.

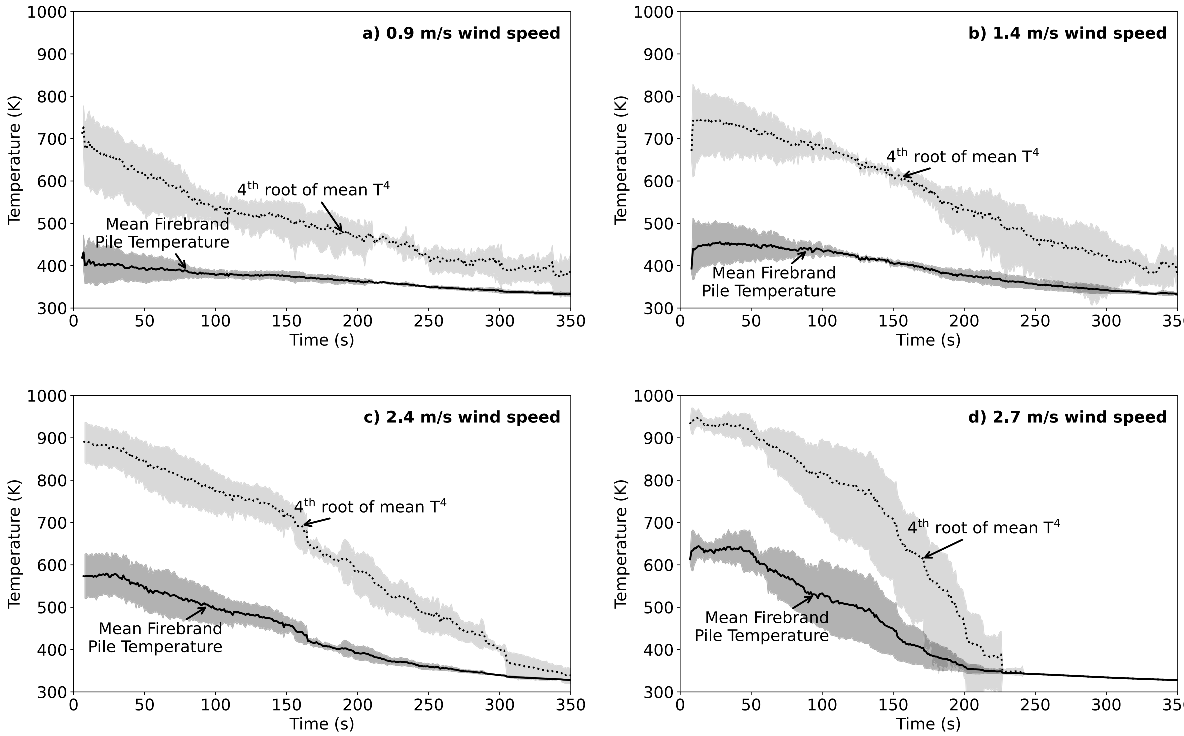

Fig. 6. Mean temperature of the rectangular firebrand pile area and corresponding mean T^4 temperature for wind speeds from 0.9 m/s to 2.7 m/s. Shaded areas indicate ± one standard deviation. t = 0 s marks wind tunnel closure.

3. Results

3.1. Ratio pyrometry

Glowing firebrands were reproducibly generated with minimal ash accumulation. No visible flame or smoke formation was observed during the wind tunnel tests, ensuring an unobstructed view to the HFG and camera. Images were acquired without external illumination. The measured surface temperature of the firebrands during the experiments at a given wind speed varied with the location within the pile and was strongly time dependent, with t = 0 s defined as the moment when the test section was closed with the borosilicate glass window. Fig. 4 shows a representative RGB image together with the corresponding surface temperature distribution of the firebrand pile obtained by ratio pyrometry at 2.7 m/s and t = 10 s. The surface temperature field exhibited localized hot and cold regions. Color ratio pyrometry captures these variations, showing that firebrands exposed to the wind glow more intensely and with higher temperatures.

The fraction of detected pixels within the pile area is governed by the spatial distribution of firebrands and their glowing intensity. Saturated pixels accounted for less than 1% within the pile area across all wind speeds. Firebrands that are non-glowing or weakly glowing are too dark to be detected or fall outside the calibration range due to their measured temperature below 873 K. Accordingly, the maximum detected fraction within the pile deposition area ranged from 15–16% at wind speeds of 0.9 and 1.4 m/s. With increasing wind speed, higher combustion intensity and temperatures resulted in a larger fraction of glowing firebrands, reaching 30% and 37% at 2.4 and 2.7 m/s, respectively.

Considering only the glowing regions of the firebrand pile, the temperature probability density function at t = 10 s for one representative test of each of the four wind speeds is shown in Fig. 5. Lower wind speeds result in broader distributions at lower temperatures, whereas higher wind speeds lead to narrower distributions shifted toward higher temperatures. The mean glowing firebrand temperature increased with wind speed, ranging from 1132 K to 1260 K. Consistent with the present results, surface temperatures of glowing regions have been reported in the range of 1020–1245 K for individual firebrands [13,17,18], and 970–1375 K for firebrand piles [20].

As a first estimate of the heat contribution from the undetected regions, thermocouple measurements of the Kaowool board surface, shown in Fig. 3, were used to characterize its heating. Since these measurements are localized and taken at a distance from the firebrand pile, they provide a lower-bound estimate of the temperature contribution of the surrounding area, with the maximum observed temperature reaching 353 K ± 12 K after 120 s. The mean temperature over the entire rectangular pile area, including the measured average Kaowool board temperature profile for non-glowing regions, is shown in Fig. 6. Owing to the fourth-power dependence of the radiative heat flux on temperature, the mean T^4 temperature

$$\overline{T^4} = \frac{1}{N}\sum_{i=1}^{N} T_i^4 \qquad (4)$$

was also calculated and plotted in Fig. 6, where N is the total number of pixels i within the firebrand pile region. The latter is consistently higher, emphasizing the influence of localized hot regions.

The results show that the firebrand temperature reaches its peak at the beginning, near $t = 0$ s, and decreases monotonically over the course of the experiment as the firebrands gradually burn out. The maximum average pile temperature increases with wind speed but also declines more rapidly, indicating faster and more intense combustion under stronger airflow due to enhanced oxygen supply. Toward the end of the tests, more firebrands remained visibly glowing for longer periods at lower wind speeds (0.9 and 1.4 m/s), whereas at higher wind speeds, the pile was consumed more quickly within the same timeframe. Uncertainties of the temperature profiles are presented as ± standard deviation of the mean.

3.2. Heat fluxes

Heat fluxes were calculated for each pixel of the image based on the measured temperatures. The integration of the spectral emissive power, as defined in Eq. (1), yields the total hemispherical emissive power of a blackbody E_b, which represents the radiative heat flux emitted over all wavelengths of the electromagnetic spectrum [29]. According to the Stefan–Boltzmann law, E_b is proportional to the fourth power of the absolute temperature, as shown in Eq. (5):

$$E_b = \int_0^\infty E_{b,\lambda}\, d\lambda = \sigma T^4, \tag{5}$$

where $\sigma = 5.67 \times 10^{-8}\ \mathrm{W/m^2K^4}$ is the Stefan–Boltzmann constant.

For real surfaces, imperfections such as ash and smoke cause the radiative emission to deviate from that of an ideal blackbody. Assuming that the emissivity ε and the transmittance τ through ash and smoke are independent of wavelength, the E_b is reduced by the factor $\varepsilon\tau$.

For the surface regions of the Kaowool board ε is given as illustrated in Fig. 3 with $\tau = 1$. For glowing firebrand regions, $\varepsilon\tau$ was initially estimated following the method of Ref. [13], which derives emissivity from the measured pyrometry temperatures. This pixel-wise emissivity extraction introduced strong variability, for which it is unclear whether it reflects physical effects or noise propagation. The method yielded an average emissivity of 0.8, consistent with the documented range of 0.73–1.0 for firebrands and charred wood surfaces [13,30]. Therefore, the average emissivity of 0.8 was applied in the following calculations to ensure that spatial variations in the heat flux are dominated by temperature rather than emissivity variations.

In this study, the incident radiative heat flux from the firebrand pile and surroundings to the HFG is to be determined. For this purpose, both surfaces are modeled as parallel gray surfaces, neglecting the surface roughness of the firebrand pile. The amount of radiative energy exchanged between two surfaces depends on their geometry, including surface area, distance, and relative orientation. These spatial relationships are expressed mathematically using view factors [31].

For two infinitesimal surface elements dA_i and dA_j, the differential view factor is defined as [31]:

$$dF_{dA_i \to dA_j} = \frac{\text{diffuse energy leaving } dA_i \text{ intercepted by } dA_j}{\text{total diffuse energy leaving } dA_i}. \tag{6}$$

Each differential radiating element dA_i corresponds to a pixel in the recorded image. The HFG was discretized into elements dA_j.

Assuming diffuse emission, i.e., uniform radiation into the hemisphere without reflection, the exchange between two differential elements is shown in Fig. 7. The differential view factor between two infinitesimal surface elements is [31]:

$$dF_{dA_i \to dA_j} = \frac{\cos(\theta_i)\cos(\theta_j)}{\pi S^2}\, dA_j, \tag{7}$$

where θ_i and θ_j are the angles between the surface normals of dA_i and dA_j and the connecting line S, which is the distance between the two differential areas.

In the present setup (see Fig. 2), the HFG was positioned centrally above the firebrand pile at a fixed vertical distance z. The spatial distance S is calculated between a given pixel at position $(x_{x,y}, y_{x,y}, 0)$ and the center of the HFG at (x_c, y_c, z). Since both surfaces are assumed to be parallel, with the gauge normal pointing downward and the image surface normal pointing upward, it follows that $\theta_i = \theta_j = \theta$, thus:

$$dF_{ij} = \frac{\cos^2(\theta)}{\pi S^2}\, dA_j, \tag{8}$$

where $\cos(\theta) = \frac{z}{S}$.

The incident radiative flux on the gauge (E_{Sensor}) is obtained by summing the power emitted by each pixel i using the Eqs. (5) and (8):

$$E_{\mathrm{Sensor}} = \frac{\sigma}{\pi\, A_{\mathrm{gauge}}} \sum_{i=1}^{N} (\varepsilon\tau)_i\, T_i^4\, A_i \int_{A_{\mathrm{gauge}}} \frac{\cos^2(\theta_i)}{S^2}\, dA_j. \tag{9}$$

Approximating the entire gauge as a single surface element eliminates the factor A_{gauge}, reducing the expression to:

$$E_{\mathrm{Sensor}} = \frac{\sigma}{\pi} \sum_{i=1}^{N} (\varepsilon\tau)_i\, A_i \frac{\cos^2(\theta_i)}{S^2}\, T_i^4. \tag{10}$$

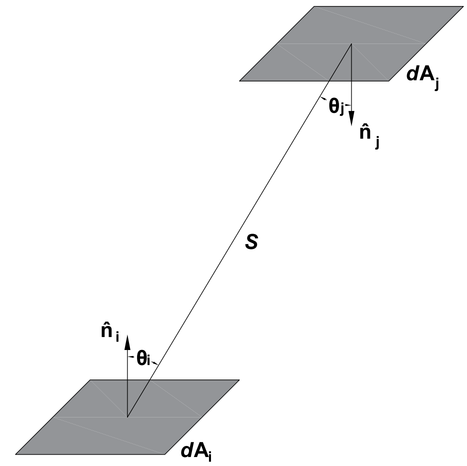

Fig. 7. Radiative exchange between two infinitesimal surface elements.

To validate the implementation of the pixel-wise view factor approach, a comparison was made with an analytically derived closed-form solution for a uniform temperature area equal to the firebrand surface [32]. The error mainly depends on the estimation of the pixel size, which represents the real-world length covered by a single image pixel and varies with the camera–object distance. In this study, a pixel size of 4×10^{-4} m was applied, resulting in an error of 0.15% compared to the pixel-independent analytical solution. For firebrand piles, the surface is not ideally planar, and $\varepsilon\tau$ was assumed uniform across the pile. Local differences in surface orientation and distance may be considered as additional sources of error.

Heat fluxes were simultaneously measured using the camera and a water-cooled HFG positioned as shown in Fig. 2, with results presented in Fig. 8. Peak values from the HFG measurement occurred between 15–18 s after tunnel closure, reaching nearly 6 kW/m^2 ± 0.3 kW/m^2 (mean ± standard deviation) at 2.7 m/s. Convective heating of the HFG was minimal due to the constant ambient-temperature airflow, with thermocouple measurements at the HFG location showing a maximum temperature increase of only 9 K. Peak heat fluxes increased linearly with wind speed, in agreement with the observations of Hakes et al. [11], who reported faster and more intense combustion under higher oxygen supply conditions at higher wind speeds.

The HFG captures radiation from the entire pile and the surrounding Kaowool board surface, including cooler regions that remain below the visible threshold ($T < 873$ K) due to their low radiative intensity. These contributions arise from hot, non-glowing firebrands and the heated surrounding Kaowool board surfaces. Thermocouple measurements on the Kaowool board, placed as illustrated in Fig. 3, reached a maximum average temperature of 353 K ± 12 K (mean ± standard deviation of the four thermocouples) after 140 s. Therefore, as a lower-bound estimate, the measured average temperature profile of the board was applied to pixels within the boundary region shown in green in Fig. 3 when they were not identified as glowing regions within the calibration range. Non-glowing pixels of the unpainted Kaowool board outside this boundary region were set to ambient temperature (298 K).

Camera-based heat fluxes exhibited a similar wind–speed dependence as the HFG measurements, with increasing peak fluxes at higher wind speeds (Fig. 8). Pyrometry values were consistently lower than HFG measurements. The relative maximum error, calculated as the peak absolute difference normalized by the HFG peak, decreased from 51% at 0.9 m/s to 20% at 2.7 m/s. The mean relative error over the 350 s measurement period was 20, 15, 12, and 10% for 0.9, 1.4, 2.4, and 2.7 m/s, respectively, reflecting improved agreement at higher wind speeds due to higher signal intensity and a larger fraction of glowing regions captured by the camera.

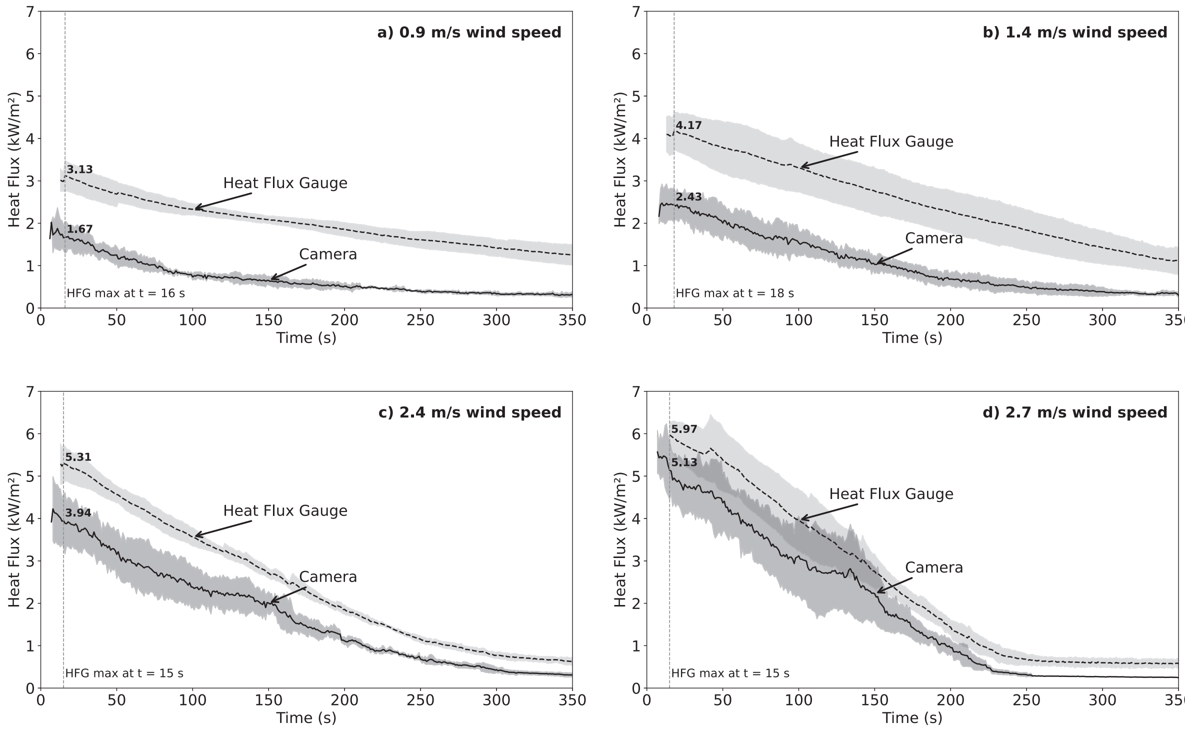

Fig. 8. Mean heat flux measured by the heat flux gauge and calculated heat flux from ratio pyrometry, both referenced to the gauge position, at wind speeds from 0.9 to 2.7 m/s. Shaded areas indicate ± one standard deviation. $t = 0$ s marks wind tunnel closure.

The observed errors primarily represent the calibration limitation of the camera with a temperature range of reliable measurements between 873 K and 1473 K. Since regions within the wind tunnel test section are partially covered by firebrands below the lower calibration temperature, radiation emitted by them is not captured by the camera. With increasing wind speed, the fraction of glowing pixels increases due to higher radiative intensity, and as a result, the error in the heat flux measurements decreases. Additionally, the HFG integrates radiation over a wider field of view, including contributions from transported firebrands outside the camera frame, whereas pyrometry is limited to the imaged pile region.

To assess the potential contributions of undetectable regions to the measured heat flux, a temperature adjustment was applied to regions not detected by the camera. First, the boundary region to which the thermocouple measurement profile was applied was manually adjusted to account for its thermal contribution, with stepwise increases implemented. An increase of 250 K above ambient temperature corresponds to an additional incident heat flux at the HFG of 0.50–0.53 kW/m^2, while a correction of +400 K results in 1.32–1.40 kW/m^2. An initial average temperature of approximately 673 K in non-glowing areas is required to align pyrometry-based fluxes with HFG measurements.

Because non-glowing areas heat up and cool down during the experiment, a constant background temperature may not be adequate. The background temperature was therefore scaled dynamically based on 40% of the average glowing firebrand temperature preserving the overall temporal evolution of the temperature throughout the test. The adjusted temperatures remain below the lower calibration threshold of 873 K, thereby still representing undetectable regions while accounting for their high temperatures. The resulting pyrometry-based heat fluxes, shown in Fig. 9, exhibit improved agreement with HFG measurements. The maximum relative error is reduced by 22% at 0.9 m/s, where the detection rate is lowest and most pixels are affected. At 2.7 m/s, the maximum relative error is 19%. Over the 350 s measurement period, the mean relative error decreases to 9, 7, 6, and 5% for the wind speeds from 0.9 to 2.7 m/s, respectively. These results demonstrate that undetected regions contribute considerably to the camera-derived heat flux measurements, as accounting for hot regions below the calibration limit strongly reduces the discrepancy with the HFG measurements.

3.3. Radiative loss fraction

The detailed temperature distribution obtained through color ratio pyrometry allows the measurement of the total outgoing radiative power (P_{out}) from the top surface of the firebrand pile. By applying the Stefan–Boltzmann law as shown in Eq. (5), P_{out} of the firebrand pile area can be calculated from each pixel i:

$$P_{\text{out}} = \sum_{i=1}^{N} (\varepsilon\tau)_i\, \sigma\, T_i^4\, A_i. \tag{11}$$

The mean radiative flux over the firebrand pile area was calculated as $\overline{E}_{\text{rad}} = P_{\text{out}}/A_{\text{pile}}$, applying the same surface temperature distribution used in Fig. 8. The maximum values increased with wind speed, ranging from 18 ± 5 kW/m^2 at 0.9 m/s, to 24 ± 4 kW/m^2 at 1.4 m/s, 43 ± 4 kW/m^2 at 2.4 m/s, and 53 ± 7 kW/m^2 at 2.7 m/s. These values are consistent with previously reported maximum radiative heat fluxes for both individual firebrands and firebrand piles, which typically range from 30 to 100 kW/m^2 [8,10,11,33,34].

The radiative loss fraction, $\chi_r = P_{\text{out}}/\text{HRR}$, was analyzed, accounting for radiative losses from the top surface of the firebrand pile area. Values were primarily documented for fuel beds during wildfire spread in laboratory settings, where radiative fractions of 0.1–0.4 have been reported [35]. For ember beds after flame extinction, values of 0.073–0.133 were measured [36].

The HRR was obtained from carbon oxide calorimetry as presented in Ref. [21] using CO and CO_2 concentrations and is shown in Fig. 10(a) for wind speeds of 0.9–2.7 m/s. Following tunnel closure (t = 0 s), HRR increased gradually, peaking between 23–30 s as oxygen supply increased with wind. Peak HRR rose from 0.3 kW at 0.9 m/s to 0.9 kW at 2.7 m/s, consistent with higher combustion intensity at stronger winds, and mirrored the trend observed in heat flux measurements. HRR decreased over time as firebrands were consumed, reaching values below 0.2 kW after approximately 150 s.

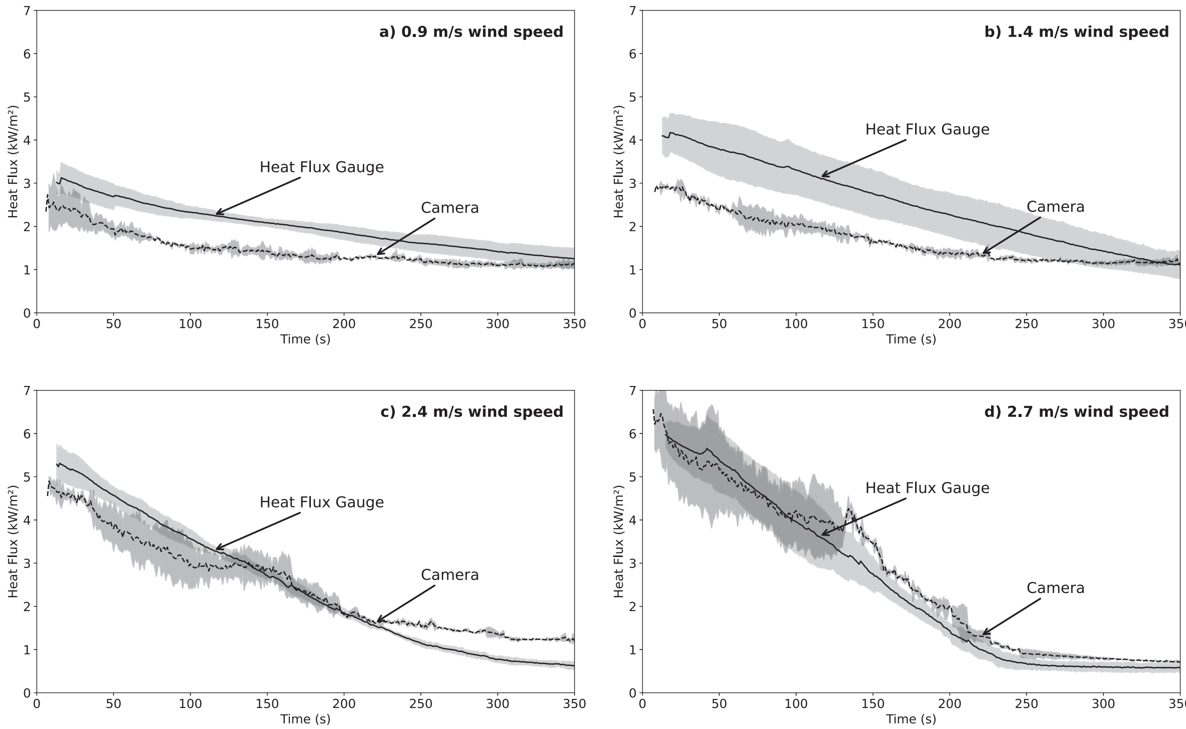

Fig. 9. Mean heat flux measured by the heat flux gauge and calculated from ratio pyrometry at wind speeds from 0.9 to 2.7 m/s, with the temperature in the boundary region increased by 0.4 times the mean temperature of the glowing firebrand region. Shaded areas indicate ± one standard deviation. t=0 s marks wind tunnel closure.

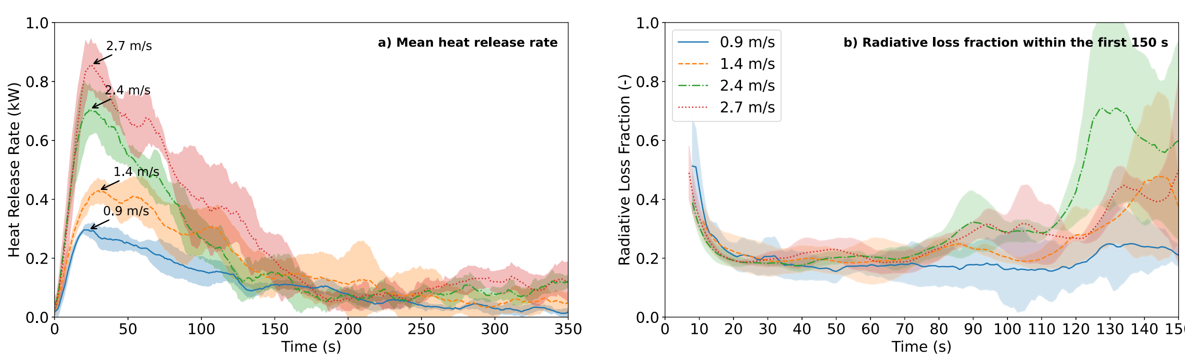

Fig. 10. (a) Mean heat release rate and (b) radiative loss fraction of the firebrand pile at 0.9–2.7 m/s. The radiative loss fraction is based on the camera-derived radiative power. Shaded areas indicate ± one standard deviation. $t = 0$ s marks wind tunnel closure.

Fig. 10(b) shows the temporal evolution of χ_r for all wind speeds. Curves represent the mean of three repetitions, with shaded areas indicating ± one standard deviation. A 2 s moving average was applied, and the data series begin once valid measurements were available after tunnel closure and camera placement. Quantity χ_r was initially high, up to 0.5, and decreased rapidly to 0.20–0.23 within the first 10 s for all wind speeds. After the initial combustion phase until 100 s, χ_r fluctuated due to low signal-to-noise ratios at very low HRR and heat flux levels; data are therefore shown only up to 150 s. Based on the results, both surface reaction rates and heat release rates exhibit a strong nonlinear dependence on temperature. Higher wind speeds increase the surface temperature and, consequently, radiative losses. Within the measured temperature range, these effects scale similarly, resulting in an approximately constant radiative loss fraction, largely independent of the wind speed.

4. Conclusions

This study demonstrates the application of color ratio pyrometry to glowing firebrand piles, extending its use beyond single firebrands for the thermal and radiative characterization under controlled wind tunnel conditions ranging from 0.9 to 2.7 m/s. The DSLR camera was calibrated using the blackbody furnace, and image processing was performed to consistently identify glowing regions within the calibration temperature range from 873 to 1473 K. This method introduces a non-intrusive alternative to point-based temperature measurements, enabling high-resolution temperature fields of firebrand surfaces. These results were used to evaluate radiative heat flux measurements at a distance. The measurements were validated against independent data from a centrally mounted, water-cooled Schmidt–Boelter heat flux gauge above the firebrand pile. Complementary heat release rate measurements were performed, enabling estimation of the radiative loss fraction. The main findings are summarized as follows:

1. Mean surface temperatures of the glowing regions ranged from 1130 K to 1260 K, with localized hot spots predominantly on the windward side.
2. Increasing wind speed enhanced combustion intensity, with a larger fraction of glowing firebrands and a higher detection rate

for color ratio pyrometry measurements. Peak temperatures of the firebrand pile increased from 431 K to 644 K and peak radiative heat fluxes reached 6 kW/m^2 at the heat flux gauge.

3. Heat fluxes from the pixel-wise view factor analysis reproduced the temporal evolution measured by the Schmidt–Boelter gauge. Introducing contributions from non-glowing regions below 873 K reduced the mean error to 5–9% across wind speeds of 0.9–2.7 m/s.
4. The radiative loss fraction stabilized in the range of 0.20–0.23 within the first 100 s of the glowing phase, indicating that the radiative loss fraction is largely independent of wind speed.

Remote, non-intrusive measurements of heat flux provide a practical alternative to direct gauge measurements in fire experiments, enabling spatially and temporally resolved data without interfering with the combustion process. The observed reduction in error when accounting for non-glowing regions highlights the importance of properly quantifying lower-temperature areas to improve measurement accuracy. The approximately constant radiative fraction indicates a reference value for the quantification of radiative heat transfer in glowing firebrands.

CRediT authorship contribution statement

Elijah J. Igweh: Writing – original draft, Visualization, Validation, Software, Methodology, Investigation, Funding acquisition, Formal analysis. **Stanislav I. Stoliarov:** Writing – review & editing, Supervision, Resources, Methodology, Conceptualization. **Peter B. Sunderland:** Writing – review & editing, Supervision, Methodology, Conceptualization.

Declaration of competing interest

The author is a Guest Editor for Fire Safety Journal and was not involved in the editorial review or the decision to publish this article.

Acknowledgments

The authors gratefully acknowledge Prof. Bart Merci (Ghent University, Belgium) for his guidance and support. IMFSE is co-funded by the European Union (https://imfse.be/). The authors also thank Dr. Farid Alinejad and Sangkyu Lee for their technical support. Elijah Igweh would also like to gratefully acknowledge the financial support for the FRISSBE project within the European Union's Horizon 2020 research and innovation programme (GA 952395).

References

[1] Marshall Burke, Anne Driscoll, Sam Heft-Neal, Jiani Xue, Jennifer Burney, Michael Wara, The changing risk and burden of wildfire in the united states, Proc. Natl. Acad. Sci. 118 (2) (2021) http://dx.doi.org/10.1073/pnas.2011048118.

[2] Matthew W. Jones, John T. Abatzoglou, Sander Veraverbeke, Niels Andela, Gitta Lasslop, Matthias Forkel, Adam J.P. Smith, Chantelle Burton, Richard A. Betts, Guido R. Van Der Werf, Stephen Sitch, Josep G. Canadell, Cristina Santín, Crystal Kolden, Stefan H. Doerr, Corinne Le Quéré, Global and regional trends and drivers of fire under climate change, Rev. Geophys. 60 (3) (2022) http://dx.doi.org/10.1029/2020RG000726.

[3] William E. Mell, Samuel L. Manzello, Alexander Maranghides, David Butry, Ronald G. Rehm, The wildland - urban interface fire problem - current approaches and research needs, Int. J. Wildland Fire 19 (2) (2010) 238, http://dx.doi.org/10.1071/WF07131.

[4] Sara E. Caton, Raquel S.P. Hakes, Daniel J. Gorham, Aixi Zhou, Michael J. Gollner, Review of pathways for building fire spread in the wildland urban interface part I: Exposure conditions, Fire Technol. 53 (2) (2017) 429–473, http://dx.doi.org/10.1007/s10694-016-0589-z.

[5] Joan L. Pellegrino, Nelson P. Bryner, Erik L. Johnsson, Wildland-Urban Interface Fire Research Needs : Workshop Summary Report, Technical report, National Institute of Standards and Technology, 2013, http://dx.doi.org/10.6028/NIST.SP.1150.

[6] Alexander Maranghides, William E. Mell, A case study of a community affected by the witch and guejito fires, Technical report, National Institute of Standards and Technology, Gaithersburg, MD, 2009, http://dx.doi.org/10.6028/NIST.TN.1635.

[7] Samuel L. Manzello, Seul-Hyun Park, Thomas G. Cleary, Investigation on the ability of glowing firebrands deposited within crevices to ignite common building materials, Fire Saf. J. 44 (6) (2009) 894–900, http://dx.doi.org/10.1016/j.firesaf.2009.05.001.

[8] Elias D. Bearinger, Jonathan L. Hodges, Fengchang Yang, Christian M. Rippe, Brian Y. Lattimer, Localized heat transfer from firebrands to surfaces, Fire Saf. J. 120 (2021) http://dx.doi.org/10.1016/j.firesaf.2020.103037.

[9] Zhenxiang Tao, Bryce Bathras, Byoungchul Kwon, Ben Biallas, Michael J. Gollner, Rui Yang, Effect of firebrand size and geometry on heating from a smoldering pile under wind, Fire Saf. J. 120 (2021) http://dx.doi.org/10.1016/j.firesaf.2020.103031.

[10] Jacques A. De Beer, Emily L. Dietz, Stanislav I. Stoliarov, Michael J. Gollner, An empirical firebrand pile heat flux model, Fire Saf. J. 141 (2023) http://dx.doi.org/10.1016/j.firesaf.2023.104004.

[11] Raquel S.P. Hakes, Hamed Salehizadeh, Matthew J. Weston-Dawkes, Michael J. Gollner, Thermal characterization of firebrand piles, Fire Saf. J. 104 (2019) 34–42, http://dx.doi.org/10.1016/j.firesaf.2018.10.002.

[12] Joe Urbas, William J. Parker, Gerald E. Luebbers, Surface temperature measurements on burning materials using an infrared pyrometer: accounting for emissivity and reflection of external radiation, Fire Mater. 28 (1) (2004) 33–53, http://dx.doi.org/10.1002/fam.844.

[13] Dennis K. Kim, Peter B. Sunderland, Fire ember pyrometry using a color camera, Fire Saf. J. (ISSN: 03797112) 106 (2019) 88–93, http://dx.doi.org/10.1016/j.firesaf.2019.04.006.

[14] H. Zhao, N. Ladommatos, Optical diagnostics for soot and temperature measurements in diesel engines, Elsevier Sci. Ltd (1998) http://dx.doi.org/10.1016/S0360-1285(97)00033-6.

[15] F. Zander, Surface temperature measurements in hypersonic testing using digital single-lens reflex cameras, J. Thermophys. Heat Transfer 30 (4) (2016) 919–925, http://dx.doi.org/10.2514/1.T4820.

[16] John M. Densmore, Matthew M. Biss, Kevin L. McNesby, Barrie E. Homan, High-speed digital color imaging pyrometry, Appl. Opt. 50 (17) (2011) http://dx.doi.org/10.1364/AO.50.002659.

[17] James L. Urban, Michela Vicariotto, Derek Dunn-Rankin, A. Carlos Fernandez-Pello, Temperature measurement of glowing embers with color pyrometry, Fire Technol. 55 (3) (2019) 1013–1026, http://dx.doi.org/10.1007/s10694-018-0810-3.

[18] Xiaoyu Ju, Michael Lisano, Mohammadhadi Hajilou, Peter B. Sunderland, Stanislav I. Stoliarov, Lizhong Yang, Michael J. Gollner, Quantification of firebrand generation from WUI fuels for model development: Firebrand generation rate, surface temperature and heat release rate, Proc. Combust. Inst. 40 (1–4) (2024) http://dx.doi.org/10.1016/j.proci.2024.105729.

[19] James H. Baldwin, Peter B. Sunderland, Ratio pyrometry of emulated firebrand streaks, Fire Saf. J. 136 (2023) http://dx.doi.org/10.1016/j.firesaf.2023.103746.

[20] Luqing Zhu, James L. Urban, Analyzing the ignition capabilities of glowing firebrand accumulations, Proc. Combust. Inst. 40 (1–4) (2024) http://dx.doi.org/10.1016/j.proci.2024.105746.

[21] Jacques De Beer, Joseph Alascio, Stanislav Stoliarov, Michael Gollner, Analysis of the thermal exposure and ignition propensity of a lignocellulosic building material subjected to a controlled deposition of glowing firebrands, Fire Saf. J. 135 (2022) http://dx.doi.org/10.1016/j.firesaf.2022.103720.

[22] Alec Lauterbach, Sangkyu Lee, Jacques De Beer, Stanislav I. Stoliarov, Peter B. Sunderland, Michael J. Gollner, Alexander I. Filkov, Gavin P. Horn, Ignition and combustion behavior of pressure treated wood and wood-plastic composite exposed to glowing firebrand piles: Impact of air flow velocity, firebrand coverage density and pile orientation, Fire Saf. J. 147 (2024) http://dx.doi.org/10.1016/j.firesaf.2024.104198.

[23] Joseph Anthony Alascio, Firebrand Pile Thermal Characterization and Ignition Study of Firebrand Exposed Wester Red Cedar, Master's Thesis. University of Mayland, Department of Fire Protection Engineering, 2021.

[24] William M Pitts, Annageri V Murthy, John L de Ris, Kjell Nyga, Debbie Smith, Ingrid Wetterlund, Round robin study of total heat flux gauge calibration at fire laboratories, Fire Saf. J. 41 (2006) http://dx.doi.org/10.1016/j.firesaf.2006.04.004.

[25] Advancing Standards Transforming Markets, Test methods for direct moisture content measurement of wood and wood-based materials, 2020, http://dx.doi.org/10.1520/D4442-20.

[26] Sony RX10 III with F2.4-4 large-aperture 24-600mm zoom lens, 2025, URL https://www.sony.co.uk/electronics/cyber-shot-compact-cameras/dsc-rx10m3/specifications. (Accessed 14 January 2025).

[27] Sneh Deep, Yedhu Krishna, Gopalan Jagadeesh, Temperature characterization of a radiating gas layer using digital-single-lens-reflex-camera-based two-color ratio pyrometry, Appl. Opt. 56 (30) (2017) http://dx.doi.org/10.1364/AO.56.008492.

[28] GitHub - ncruces/dcraw: Mirror of dave coffin's dcraw, with full history, 2025, URL https://github.com/ncruces/dcraw/tree/master. (Accessed 2 February 2025).

[29] Adrian Bejan, Heat Transfer, John Wiley & Sons, Inc., 1993.
[30] Michael J. Spearpoint, James G. Quintiere, Predicting the piloted ignition of wood in the cone calorimeter using an integral model - effect of species, grain orientation and heat flux, Fire Saf. J. 4 (36) (2001) 391–415, http://dx.doi.org/10.1016/S0379-7112(00)00055-2.
[31] M.F. Modest, Radiative heat transfer, third ed., Academic Press, New York, ISBN: 978-0-12-386944-9, 2013.
[32] Robert Siegel, John Howel, Thermal Radiation Heat Transfer, fourth ed., Taylor & Francis, ISBN: 1-56032-839-8, 2001.
[33] Amy E. Mensch, Savannah S. Wessies, Anthony Hamins, Jiann C. Yang, Measuring firebrand heat flux with a thin-skin calorimeter, Fire Saf. J. 140 (2023) http://dx.doi.org/10.1016/j.firesaf.2023.103859.
[34] Hamed Salehizadeh, Raquel S.P. Hakes, Michael J. Gollner, Critical ignition conditions of wood by cylindrical firebrands, Front. Mech. Eng. 7 (2021) http://dx.doi.org/10.3389/fmech.2021.630324.
[35] Alexander I. Filkov, Virginie Tihay-Felicelli, Nima Masoudvaziri, David Rush, Andres Valencia, Yu Wang, David L. Blunck, Mario Miguel Valero, Kamila Kempna, Jan Smolka, Jacques De Beer, Zakary Campbell-Lochrie, Felipe Roman Centeno, Muhammad Asim Ibrahim, Calisa Katiuscia Lemmertz, Wai Cheong Tam, A review of thermal exposure and fire spread mechanisms in large outdoor fires and the built environment, Fire Saf. J. 140 (2023) 103871, http://dx.doi.org/10.1016/j.firesaf.2023.103871.
[36] Frédéric Morandini, Yolanda Perez-Ramirez, Virginie Tihay, Paul-Antoine Santoni, Toussaint Barboni, Radiant, convective and heat release characterization of vegetation fire, Int. J. Therm. Sci. 70 (2013) 83–91, http://dx.doi.org/10.1016/j.ijthermalsci.2013.03.011.